An Estimator for Weather Radar Doppler Power Spectrum via Minimum Mean Square Error

Eiichi Yoshikawa, Naoya Takizawa, Hiroshi Kikuchi, *Member, IEEE*, Tomoaki Mega, and Tomoo Ushio, *Senior Member, IEEE*

***Abstract*— This article proposes a method for estimating the Doppler power spectrum (DPS) of a weather radar via minimum mean square error (MMSE). In order to detect severe weather phenomena that mostly occur within the lowest few kilometers of the atmosphere, weather radars have to direct their beams at low elevation angles, and the received signals from such observations usually contain reflections from the ground and buildings, so-called ground clutter. The MMSE estimator, which is an adaptive spectral estimator, allows weather radar DPSs to be obtained with excellently reduced ground clutter contaminations. The MMSE estimator was examined by numerical simulations, which supposed various precipitation and ground clutter scenarios and DPS estimation parameter values. The MMSE estimator provided DPSs almost as accurate as those from the traditional Fourier and windowed Fourier estimators in simulations with no ground clutter and much better DPSs than those estimators in the presence of ground clutter. Furthermore, the MMSE estimator gave better suppression of ground clutter contamination than the Capon estimator, which is another adaptive spectral estimator. As a result of statistical evaluations, ground clutter signals with a strong clutter-to-noise ratio of 70 dB appeared only in a narrow velocity range of the MMSE DPS, from −2 to 2 m/s, and caused degradation of the mean and standard errors outside this velocity range by just 1 dB. The MMSE estimator was also applied to signals received by actual weather radar, and DPS estimation of precipitation signals with similarly low ground clutter contamination was demonstrated.**

***Index Terms*— Adaptive filter, Doppler spectrum, weather radar.**

I. Introduction

A WEATHER radar's Doppler power spectrum (DPS) represents the Doppler velocity profile of power received from hydrometeors in a target volume and is typically output by current weather radars. A weather radar's range from tens to hundreds of kilometers gives it many advantages over spot anemometer observations, and radar Doppler velocity measurements are widely used to reduce or avoid severe weather damage in various applications [1].

Severe weather is occurring more frequently than in the past and bringing greater risks, particularly to urban areas. Therefore, there is an increasing demand for early detection and warning of severe weather phenomena, for which we purpose that a network of small weather radars is better than a single long-range weather radar [2]. Chandrasekar *et al.* [3] deployed a network of X-band weather radars in the Dallas-Fort Worth area that had various practical applications. In Japan, X-band weather radars have been deployed nationwide, and redundant observations are being made of urban areas in particular [4]. A network of Ku-band weather radars, which have very localized coverage of a few tens of kilometers and a very high range resolutions on the order of several meters, has been constructed and evaluated for research purposes [5]–[7]. Furthermore, an X-band phased array weather radar (PAWR) designed specifically for severe weather detection with a high temporal resolution of 30 s for a full-volume scan has been developed and is now in test operation [8].

When observing urban areas, weather radar DPSs are heavily contaminated by ground clutter due to the high concentrations of buildings. Moreover, the contamination becomes more serious when observing at the lower elevation angles where severe weather occurs. Even outside urban areas, both precipitation and ground clutter signals typically appear in the DPSs of many observations. While precipitation signals span a wide range of Doppler velocities, ground clutter appears in a narrow band of velocity components around the zero velocity [9]. Most weather radars use a signal processing method to filter DPSs for eliminating ground and sea clutter, erroneous outliers, and so on. For ground clutter suppression, near-zero-velocity components in DPSs are cut and filled by considering the continuity of velocity components [11]. This method can almost completely extract a pure precipitation signal from a DPS when it does not overlap with a ground clutter signal. In a DPS in which these overlap, however, near-zero-velocity components of the precipitation signal are discarded when the ground clutter signal is removed and cannot, in principle, be completely repaired.

The traditional DPS estimator is based on the Fourier method. When strong ground clutter exists, heavy contamination caused by sidelobes are present in all velocity components of a DPS and smear any precipitation signal (so-called spectral leakage). The filtering method described above cannot be successfully applied in this case. Although a windowed Fourier

Manuscript received April 28, 2019; revised October 23, 2019, March 15, 2020, July 14, 2020, and September 11, 2020; accepted November 27, 2020. Date of publication January 15, 2021; date of current version December 3, 2021. This work was supported by JSPS KAKENHI under Grant JP17H02069. *(Corresponding author: Eiichi Yoshikawa.)*

Eiichi Yoshikawa is with the Japan Aerospace Exploration Agency, Mitaka 181-0015, Japan (e-mail: yoshikawa.eiichi@jaxa.jp).

Naoya Takizawa is with Tokyo Metropolitan University, Hino 191-0065, Japan.

Hiroshi Kikuchi is with the Center for Space Science and Radio Engineering (SSRE), The University of Electro-Communications, Chofu 182-8585, Japan.

Tomoaki Mega and Tomoo Ushio are with the Department of Electrical Engineering, Osaka University, Suita 565-0871, Japan.

Digital Object Identifier 10.1109/TGRS.2020.3044111

This work is licensed under a Creative Commons Attribution-NonCommercial-NoDerivatives 4.0 License.
For more information, see https://creativecommons.org/licenses/by-nc-nd/4.0/

method can obtain a DPS with reduced sidelobes, it broadens both the ground clutter and precipitation signals in the DPS. A widened ground clutter mainlobe has a higher probability of overlapping with a precipitation spectrum, and when such overlap occurs, the precipitation signal is heavily degraded by the removal of many near-zero velocity components. Even when there is no overlap, the precipitation signal is distorted by the spectral broadening. This article defines "spectral broadening" as an effect that broadens a DPS as the result only of the DPS estimation process. More generally, "spectral broadening" occurs not only due to the DPS estimation process but also due to turbulence, variations of hydrometeor movements, and so on. For general spectral estimation, it is well known that adaptive estimators, such as the Capon method [12], can effectively suppress sidelobes without causing spectral broadening.

This article proposes a method of adaptive DPS estimation via a minimum mean square error (MMSE) framework. The MMSE framework was proposed in our previous research on phased array digital beamforming and realized the estimation of the precise angle profile of received power by excellently suppressing antenna sidelobes [13]. Since the Doppler spectral analysis is in principle equivalent to phased array beamforming, as explained in Appendix A, it is analogously expected that a DPS estimator via MMSE can suppress ground clutter contamination caused by sidelobes and can make a precipitation signal detectable and correctly estimable even in the presence of strong ground clutter.

In the following, Section II presents a signal model of weather radar Doppler spectral analysis as a preface. The methodology of the MMSE estimator is elaborated in Section III, in which the traditional Fourier and windowed Fourier estimators and the Capon estimator are also explained. In Section IV, the characteristics of the MMSE estimator are compared with the traditional estimators, and its accuracies are statistically evaluated by numerical simulation. In Section V, MMSE-estimated DPSs calculated from actual weather radar observation signals are presented. Section VI discusses the dependencies of estimation accuracy on detailed parameters of the MMSE process. Section VII concludes this article.

II. Signal Model

A weather radar typically emits pulses at a repetition frequency [pulse repetition frequency (PRF)] of several kilohertz and receives pulses backscattered by hydrometeors. A signal from hydrometeors in a target volume (that is, in a gate at a desired distance) is obtained by sampling the received signal at the PRF with a delay time corresponding to distance. The signal due to a single moving hydrometeor is supposed to appear in the received signal as a constant-frequency wave, the properties of which are determined by a complex amplitude and the Doppler velocity of the hydrometeor. The principle of superposition gives the received signal from multiple hydrometeors as the summation of the signals of each individual hydrometeor, expressed as

$$\boldsymbol{y} = \sum_{\nu \in \boldsymbol{\Omega}} \chi_\nu \boldsymbol{\theta}_\nu + \boldsymbol{n} \tag{1}$$

where $\boldsymbol{y}$ denotes a received signal at an arbitrary distance (delay time), which is digitized into N samples as

$$\boldsymbol{y} = \begin{bmatrix} y^{(1)} & y^{(2)} & \dots & y^{(n)} & \dots & y^{(N)} \end{bmatrix}^{\mathrm{T}}.$$

N is also the number of transmitted pulses. χ_ν depends on the complex scattering amplitude of the νth hydrometeor in the target volume. $\boldsymbol{\theta}_\nu$ is a constant-frequency wave corresponding to the νth hydrometeor, represented as

$$\boldsymbol{\theta}_\nu = \begin{bmatrix} \theta_\nu^{(1)} & \theta_\nu^{(2)} & \dots & \theta_\nu^{(n)} & \dots & \theta_\nu^{(N)} \end{bmatrix}^{\mathrm{T}}$$

where $\theta_\nu^{(n)} = \exp(j2\pi f_\nu n \Delta_t)$ and f_ν is the Doppler frequency shift due to the motion of the νth hydrometeor. Δ_t is the discretization step size (the reciprocal of the PRF). $\boldsymbol{\Omega}$ represents a set of hydrometeors in a target volume. $\boldsymbol{n}$ is an N-vector of additive noise which is supposed to be a complex normal random. Specifically, $\mathrm{E}[\boldsymbol{n}] = \boldsymbol{0}$, and $\mathrm{E}[\boldsymbol{n}\boldsymbol{n}^{\mathrm{H}}] = \sigma_n^2 \boldsymbol{I}$.

The received signal from a target volume can be approximated as

$$\boldsymbol{y} \approx \sum_{m=-M/2}^{M/2-1} x_m \boldsymbol{s}_m + \boldsymbol{n} \tag{2}$$

where

$$x_m = \sum_{\nu \in \boldsymbol{\Omega}_m} \chi_\nu$$

and

$$\boldsymbol{s}_m = \begin{bmatrix} s_m^{(1)} & s_m^{(2)} & \dots & s_m^{(n)} & \dots & s_m^{(N)} \end{bmatrix}^{\mathrm{T}}.$$

$s_m^{(n)} = \exp(j2\pi m \Delta_f n \Delta_t)$ is defined. $\boldsymbol{\Omega}_m$ represents a set of hydrometeors that have Doppler shifts from $(m - 1/2)\Delta_f$ to $(m + 1/2)\Delta_f$. Δ_f $(\leq (N\Delta_t)^{-1})$ must be sufficiently small. Now, 2 can be expressed in the matrix form as

$$\boldsymbol{y} \approx \boldsymbol{S}\boldsymbol{x} + \boldsymbol{n} \tag{3}$$

where

$$\boldsymbol{S} = \begin{bmatrix} \boldsymbol{s}_{-M/2} & \boldsymbol{s}_{-M/2+1} & \dots & \boldsymbol{s}_m & \dots \boldsymbol{s}_{M/2-1} \end{bmatrix}$$

and

$$\boldsymbol{x} = \begin{bmatrix} x_{-M/2} & x_{-M/2+1} & \dots & x_m & \dots & x_{M/2-1} \end{bmatrix}^{\mathrm{T}}.$$

When $M = N = (\Delta_t \Delta_f)^{-1}$, $\boldsymbol{S}$ is a row-switching transformation of the inverse Fourier matrix. When $M \geq (\Delta_t \Delta_f)^{-1} \geq N$, furthermore, 2 and 3 become equalities because $\boldsymbol{\theta}_\nu$ can be decomposed by a Fourier series of $\boldsymbol{S}$.

III. Doppler Spectral Estimators

Doppler spectral estimation is expressed by

$$\boldsymbol{x}^{[\mu]} = \boldsymbol{W}^{[\mu]\mathrm{H}} \boldsymbol{y} \tag{4}$$

where $\boldsymbol{x}^{[\mu]}$ is an estimated (complex) spectrum. An estimated DPS can be obtained by applying the absolute square function to each element of $\boldsymbol{x}^{[\mu]}$. $\boldsymbol{W}^{[\mu]}$ is a matrix for Doppler spectral analysis that is determined by an estimator. In this article, the superscript $[\mu]$ denotes the type of estimator: $[f]$: Fourier estimator; $[h]$: windowed Fourier estimator; $[c]$: Capon estimator; or $[m]$: MMSE estimator. These four estimators are

categorized as nonparametric spectral estimators because they do not assume any models on signals $\boldsymbol{y}$. Parametric spectral estimators that assume a parametric random process model are also well known. A typical method of such parametric spectral estimators is based on an autoregressive (AR) model [14, Ch. 3], which is discussed in conjunction with weather radar received signals in [1, Ch. 20a]. This article briefly compares the MMSE estimator to the AR estimator in Appendix B.

A. Fourier and Windowed Fourier Estimators

Fourier estimation is the fundamental approach for Doppler spectral analysis. A Fourier spectrum $\boldsymbol{x}^{[f]}$ is estimated by

$$\boldsymbol{x}^{[f]} = \boldsymbol{W}^{[f]\mathrm{H}}\boldsymbol{y} \tag{5}$$

where

$$\boldsymbol{W}^{[f]\mathrm{H}} = \frac{1}{N}\boldsymbol{A}^{\mathrm{H}}.$$

$\boldsymbol{A}$ is defined as

$$\boldsymbol{A} = \begin{bmatrix}\boldsymbol{a}_{-M'/2} & \boldsymbol{a}_{-M'/2+1} & \dots & \boldsymbol{a}_{m'} & \dots & \boldsymbol{a}_{M'/2-1}\end{bmatrix}$$
$$\boldsymbol{a}_{m'} = \begin{bmatrix}a_{m'}^{(1)} & a_{m'}^{(2)} & \dots & a_{m'}^{(n)} & \dots & a_{m'}^{(N)}\end{bmatrix}^{\mathrm{T}}$$

where $a_{m'}^{(n)} = \exp(j2\pi m'\Delta'_f n\Delta_t)$. The primes indicate that Δ_f and M (and m) are obtained from the weather radar's specifications and are not necessarily the same as those in the signal model. A Fourier DPS is calculated by applying the absolute square to each element of $\boldsymbol{x}^{[f]}$.

To mitigate velocity sidelobes that occur in $\boldsymbol{x}^{[f]}$, the received signal may be multiplied with a window function prior to Fourier estimation. A windowed Fourier spectrum $\boldsymbol{x}^{[h]}$ is estimated by

$$\boldsymbol{x}^{[h]} = \boldsymbol{W}^{[h]\mathrm{H}}\boldsymbol{y} \tag{6}$$

where

$$\boldsymbol{W}^{[h]\mathrm{H}} = \boldsymbol{A}^{\mathrm{H}}\,\mathrm{diag}\,(\boldsymbol{h}).$$

$\boldsymbol{h}$ is a vector that digitally expresses the window function that is normalized as $\boldsymbol{h}^{\mathrm{T}}\boldsymbol{h} = N^{-1}$. When $\boldsymbol{h}$ is rectangular, 6 is equivalent to 5. The windowed Fourier DPS is calculated by taking the absolute square of each element of $\boldsymbol{x}^{[h]}$. It is known that, for a single velocity component, its sidelobes are suppressed, and the mainlobe is broadened in the windowed Fourier DPS compared with the (nonwindowed) Fourier DPS [9]. In practice, it is necessary to use an aggressive window function, which brings large spectral broadening, only when strong ground clutter exists.

B. Capon Estimator

The Capon estimator is also called the maximum likelihood method. It is obtained as the minimum power estimation at each arbitrary Doppler velocity, which is expressed by

$$\boldsymbol{x}^{[c]} = \boldsymbol{W}^{[c]\mathrm{H}}\boldsymbol{y} \tag{7}$$

where

$$\boldsymbol{W}^{[c]\mathrm{H}} = \{(\boldsymbol{A}^{\mathrm{H}}\boldsymbol{R}^{-1}\boldsymbol{A}) \odot \boldsymbol{I}\}^{-1}\boldsymbol{A}^{\mathrm{H}}\boldsymbol{R}^{-1}.$$
$$\boldsymbol{R} = \mathrm{E}[\boldsymbol{y}\boldsymbol{y}^{\mathrm{H}}].$$

The Capon DPS is obtained by applying the absolute square to each element of $\boldsymbol{x}^{[c]}$. E[•] indicates the expectation. The expectation has to be approximated by an finite number of received signals $\boldsymbol{y}$, and N received signals are at least necessary to invert $\boldsymbol{R}$. In weather radar DPS estimation, a single received signal is obtained at a range gate and angle. Although several similar signals can simultaneously be acquired at its adjacent range gates or adjacent angles, even with them, the number of received signals does not reach N in most weather radars. As explained in [14, Ch. 6], otherwise, an invertible $\boldsymbol{R}$ is approximately calculated with a received signal which contains $(2N-1)$ elements. To obtain $\boldsymbol{y}$ with $(2N-1)$ samples, however, weather radars have to spend longer time observing each direction.

This article instead defines a concatenated received signal as $\boldsymbol{y}^{[c]} = [\boldsymbol{y}^{\mathrm{T}} \quad \boldsymbol{y}_{a1}^{\mathrm{T}} \quad \boldsymbol{y}_{a2}^{\mathrm{T}} \quad \dots]^{\mathrm{T}}$. $\boldsymbol{y}_{a1}, \boldsymbol{y}_{a2}, \dots$ are the received signals at adjacent range gates or adjacent angles, which are simultaneously measured with $\boldsymbol{y}$. By using $\boldsymbol{y}^{[c]}$, a practical approximation for calculating $\boldsymbol{R}$ can be derived in a similar manner to [14, Ch. 6] as

$$\boldsymbol{R}^{[c]} \approx \frac{1}{N'-N+1}\sum_{n=1}^{N'-N+1}\boldsymbol{y}_n^{[c]}\boldsymbol{y}_n^{[c]\mathrm{T}} \tag{8}$$

where N' is the number of elements of $\boldsymbol{y}^{[c]}$. $\boldsymbol{y}_n^{[c]}$ is an N vector containing the nth to $(n+N-1)$th elements of $\boldsymbol{y}^{[c]}$. Similar to [14, Ch. 6], N' must be greater than or equal to $(2N-1)$ in order to make $\boldsymbol{R}^{[c]}$ invertible. In the concatenated received signal $\boldsymbol{y}_n^{[c]}$, for example, there is no correlation between the Nth and $(N+1)$th elements. This is because the Nth and $(N+1)$th elements of $\boldsymbol{y}^{[c]}$, respectively, correspond to the Nth element of $\boldsymbol{y}$ and the first element of $\boldsymbol{y}_{a1}$, and $\boldsymbol{y}$ and $\boldsymbol{y}_{a1}$ are obtained from different sets of hydrometeors. Thus, $\boldsymbol{R}^{[c]}$ does not converge to $\boldsymbol{R}$ even though N' increases.

Note that the diagonal loading method [10], which is well-known to make a covariance matrix invertible by adding a diagonal matrix with a small magnitude, is not considered in this article because it involves a problem how to determine the magnitude.

C. MMSE Estimator

A derivation of the MMSE estimator for phased array beamforming is elaborated in [13]. Applying the MMSE framework to the Doppler spectral analysis (see Appendix A for the equivalency between the phased array beamforming and the Doppler spectral analysis), MMSE estimation is carried out as the following iterative procedure:

$$\boldsymbol{x}_{(l)}^{[m]} = \boldsymbol{W}_{(l)}^{[m]\mathrm{H}}\boldsymbol{y} \tag{9}$$

where

$$\boldsymbol{W}_{(l)}^{[m]\mathrm{H}} = \left\{\left(\boldsymbol{A}^{\mathrm{H}}\boldsymbol{R}_{(l-1)}^{-1}\boldsymbol{A}\right) \odot \boldsymbol{I}\right\}^{-1}\boldsymbol{A}^{\mathrm{H}}\boldsymbol{R}_{(l-1)}^{-1}$$
$$\boldsymbol{R}_{(l-1)} = \boldsymbol{A}\boldsymbol{\Sigma}_{x(l-1)}\boldsymbol{A}^{\mathrm{H}} + \boldsymbol{\Sigma}_n$$
$$\boldsymbol{\Sigma}_{x(l-1)} = \mathrm{E}\left[\boldsymbol{x}_{(l-1)}^{[m]}\boldsymbol{x}_{(l-1)}^{[m]\ \mathrm{H}}\right].$$

$\boldsymbol{x}_{(l)}^{[m]}$ denotes the MMSE spectrum of the lth iteration, and $\boldsymbol{x}_{(0)}^{[m]} = \boldsymbol{x}^{[f]}$ is defined. As with the other estimators, the

TABLE I
SIGNAL SIMULATION PARAMETERS

Carrier Frequency		9.5 GHz
Precipitation	Spectral shape	Gaussian
	Power	0, 10, or 20 dB (SNR)
	Mean velocity	0, 1, . . ., or 19 m/sec
	Spectral width	1, 2, or 4 m/sec
Ground clutter	Spectral shape	Gaussian
	Power	$-\infty$, 30, 50, or 70 dB (CNR)
	Mean velocity	0 m/sec
	Spectral width	0.25 m/sec
Signal simulation	Nyquist Frequency ($M\Delta_f$)	20 kHz
	No. of frequency samples (M)	4,096
	PRF (Δ_t^{-1})	2.5 kHz
	No. of transmitted pulses (N)	32, 64, or 128

MMSE DPS (of the lth iteration) is calculated by applying the absolute square to each element of $\boldsymbol{x}_{(l)}^{[m]}$. $\boldsymbol{\Sigma}_{x(l)}$ is approximated to an arithmetic mean as $\overline{(\boldsymbol{x}_{(l)}^{[m]}\boldsymbol{x}_{(l)}^{[m]\mathrm{H}})} \odot \boldsymbol{I}$, where the arithmetic mean is taken over multiple independent received signals obtained from adjacent range gates or angles. $\boldsymbol{\Sigma}_n = \mathrm{E}[\boldsymbol{n}\boldsymbol{n}^{\mathrm{H}}] = \sigma_n^2 \boldsymbol{I}$ is defined, and σ_n is assumed to be known. The addition of the diagonal matrix $\boldsymbol{\Sigma}_n$ makes $\boldsymbol{R}_{(l-1)}$ invertible. The addition of $\boldsymbol{\Sigma}_n$ may look similar to the diagonal loading method. In contrast that the diagonal loading method does not determine its loading magnitude, the MMSE estimator can calculate the magnitude from the noise level. Iteration is continued until the difference between $\boldsymbol{x}_{(l)}^{[m]}$ and $\boldsymbol{x}_{(l-1)}^{[m]}$ becomes sufficiently small. This article applies an iteration termination criterion using σ_n as

$$\left\|\boldsymbol{x}_{(l)}^{[m]} - \boldsymbol{x}_{(l-1)}^{[m]}\right\|_2^2 < \delta \frac{M'}{N} {\sigma_n}^2 \tag{10}$$

where δ should be small so that the iterative updates are sufficiently smaller than the noise level.

It is noticed by comparing 7 with 9 that the Capon and MMSE estimators are quite similar and differ only in the approximate calculations of their covariance matrices, $\boldsymbol{R}^{[c]}$ (Capon) and $\boldsymbol{R}_{(l-1)}$ (MMSE). As stated in the Section III-B, the Capon estimator applies an approximation of 8, in which the vector concatenation obstructs $\boldsymbol{R}^{[c]}$ converging to $\boldsymbol{R}$. In contrast, the MMSE estimator approximates the calculation of $\boldsymbol{\Sigma}_{x(l-1)}$, which is based on an assumption that every couple of $\boldsymbol{x}_{(l)}^{[m]}$ elements are independent. The assumption in the MMSE estimator is consistent with the characteristics of the weather radar received signal.

IV. PERFORMANCE

The accuracy and computational complexity of the MMSE estimator were evaluated by numerical simulation. The simulated signals received by a weather radar were synthesized, and their DPSs were estimated. The parameters of the weather radar and the estimation processes are summarized in Tables I and II, respectively. Table I supposes a typical X-band weather radar with a carrier frequency of 9.5 GHz.

A. Signal Simulation

The simulated received signals containing precipitation and ground clutter signals were synthesized based on [15], [16]. Each DPS of a precipitation or ground clutter signal was represented by a Gaussian function with a certain parameter set. The parameter sets were varied, as shown in Table I.

The powers of precipitation and ground clutter signals were represented by relative values to the power of noise, that is, the signal-to-noise ratio (SNR) and the clutter-to-noise ratio (CNR), respectively. The frequency axis of DPSs was defined by the Nyquist frequency of 20 kHz, and the number of digital samples of the simulated received signal M was set to 4,096. In other words, the frequency axis was digitally defined from -10 to 10 kHz with a step size of 20/4096 kHz (strictly speaking, the maximum frequency was 10–20/4096 kHz.) The principle of the radar Doppler spectral analysis converts the frequency axis to a velocity axis, which was from -157.89 to 157.82 m/s with a step size of 0.08 m/s. The velocity axis covered a sufficiently wide range considering the natural Doppler velocities of precipitation and was sufficiently fine for the approximation of 2.

A complex spectrum of precipitation was generated as elementwise products of square roots of a precipitation DPS and a sequence of complex normal random numbers. A complex ground clutter spectrum was also generated in the same manner. Summation of these two complex spectra results in a simulated $\boldsymbol{x}$. Equation 3 gives a noise-added received signal in the time domain, $\boldsymbol{y}$. Here, the PRF (Δ_t^{-1}) was set to 2.5 kHz, and the number of transmitted pulses N was 32, 64, or 128. For additive noise $\boldsymbol{n}$, σ_n is relative to the powers of the precipitation and ground clutter signals.

Fig. 1 shows an example of a simulated signal. The precipitation signal in this example was defined with a power of 10 dB (SNR), a mean velocity of 4 m/s, and a spectral width of 2 m/s, and the ground clutter signal had a power of 30 dB (CNR). The absolute square of $\boldsymbol{x}$ is shown as a black line. DPSs of the precipitation and ground clutter signals, of which $\boldsymbol{x}$ consists, are shown as blue and green lines, respectively. The black line is almost overlapped by the green and blue lines.

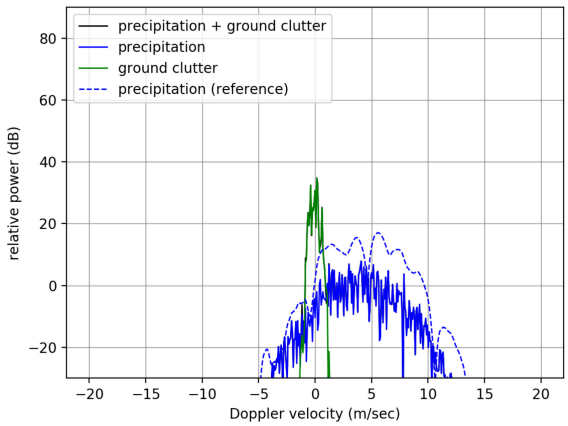

Fig. 1. Example generated signal simulating a precipitation signal of 10-dB (SNR) power, 4-m/s mean velocity, and 2.0-m/s spectral width and a 30-dB (CNR) ground clutter signal. The reference was calculated by supposing $N = 32$.

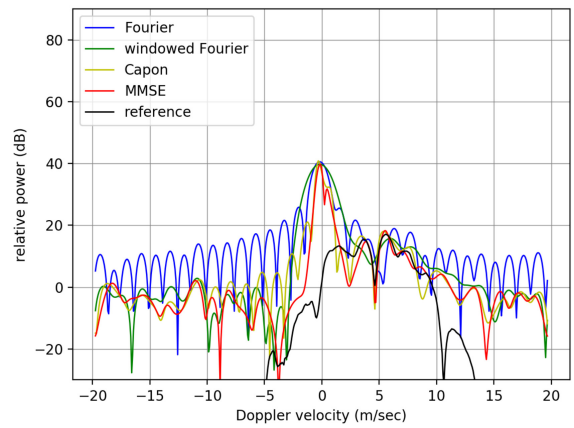

Fig. 2. Examples of DPS estimation results with $N = 32$, a precipitation signal of 10-dB (SNR) power, 4-m/s mean velocity, and 2-m/s spectral width and a ground clutter signal of 30-dB (CNR) power.

The blue dashed line indicates a DPS of precipitation, which is calculated by using a mainlobe of the Fourier estimator. Specifically, its complex DPS is calculated as

$$\boldsymbol{x}^{[t]} = \{(\boldsymbol{W}^{[f]\mathrm{H}}\boldsymbol{A}) \odot \boldsymbol{E}\}\hat{\boldsymbol{x}} \tag{11}$$

where $\hat{\boldsymbol{x}}$ denotes the complex spectrum of a precipitation signal. $\boldsymbol{E}$ is a matrix of size $\boldsymbol{W}^{[f]\mathrm{H}}\boldsymbol{A}$. Each row of $\boldsymbol{W}^{[f]\mathrm{H}}\boldsymbol{A}$ represents a (velocity) ambiguity function of the Fourier estimator, and the ambiguity function has a mainlobe and sidelobes. $\boldsymbol{E}$ works to discard the sidelobes, that is, its elements that correspond to the Fourier estimator's mainlobe are set to one; otherwise, they are zero. For Fig. 1, $\boldsymbol{x}^{[t]}$ was calculated by setting the number of transmitted pulses N to 32.

$\boldsymbol{x}^{[t]}$ is the reference DPS in weather radar DPS estimations. Radars that observe distributed targets (such as weather radars) postulate that a component of measurement contains signals from many particles (hydrometeors). As in 2, a velocity component of complex spectra is defined as the summation of complex scattering amplitudes of hydrometeors in a range of Doppler velocities $\boldsymbol{\Omega}_m$. With a weather radar, the temporal length of a received signal ($N\Delta_t$) is defined in its specification and determines an ambiguity function's mainlobe that works to sum the complex amplitudes of hydrometeors. The mainlobe depends on the DPS estimator employed, and the Fourier estimator produces a mainlobe with the minimum achievable width.

B. DPS Estimation

The specifications of DPS estimations in the simulations are summarized in Table II. The number of frequency samples M', which is a parameter of $\boldsymbol{A}$ in 5, was set to 512. Since the PRF (Δ_t^{-1}) is 2.5 kHz, the frequency axis of the estimated DPS is then from -1.25 to 1.25–2.5/512 kHz with a step size of 2.5/512 kHz. This was converted to a velocity axis from -19.74 to 19.66 m/s with a step size of 0.08 m/s. The Hamming window [17] was adopted for the windowed Fourier estimations except for cases with a large CNR of 70 dB, for which the Blackman window, which is well known to have small sidelobes, was applied. For the Capon estimator, it was assumed that five independent received signal were used, that is, $N' = 5N$. For the MMSE estimator, the same number of independent received signals was used for $\boldsymbol{R}_{(l)}$. The termination criterion of the MMSE estimator's iteration process was based on 10 with $\delta = 10^{-2}$.

Fig. 2 shows examples of DPSs estimated by the Fourier, windowed Fourier, Capon, and MMSE estimators as blue, green, yellow, and red lines, respectively. The reference (precipitation) DPS is overplotted as a black line. The DPSs were calculated from the simulated signal of Fig. 1. With the Fourier DPS, the precipitation signal is smeared by ground clutter contaminations caused by sidelobes. Although the windowed Fourier estimation reduces the sidelobes and makes the precipitation detectable, it broadens the ground clutter signal that interferes with the precipitation signal over a wide range of around-zero Doppler velocities. The Capon estimator narrows the ground clutter signal and has reduced sidelobes compared with the Fourier estimator. However, the first and second sidelobes cogenerated by the ground clutter are seen at the Doppler velocities from roughly -4 to -2 m/s. They are expected to appear on the positive velocity side at higher CNRs although they are not prominent here since they have less power than the precipitation signal. In the MMSE estimation, ground clutter contaminations due to sidelobes do not appear, and the ground clutter signal is sharply estimated and interferes with the precipitation signal only in a narrow range of around-zero Doppler velocities.

C. Accuracy

1) DPSs Without Ground Clutter: Fig. 3 shows examples of estimated DPSs without ground clutter (a CNR of $-\infty$ dB). Fig. 3(a)–(c) corresponds to the simulations with precipitation signals with powers of 10, 20, and 30 dB (SNR), respectively. In these simulations, a mean velocity of 4 m/s and a spectral width of 2 m/s were defined for the precipitation signals, and N was set to 32. The Fourier estimation accurately reproduced the reference in Fig. 3(a) because it does not produce spectral broadening, and its sidelobes are not remarkable with a

TABLE II
SPECIFICATIONS OF DPS ESTIMATION

No. of frequency samples (M')		512
Windowed Fourier estimator	Window function	Hamming or Blackman (when simulating a CNR of 70 dB)
Capon estimator	No. of independent received signals	5
MMSE estimator	No. of independent received signals	5
	Iteration termination criterion	$\delta = 10^{-2}$ in Eq. 10

precipitation signal power of 10 dB (SNR). Fig. 3(b) and (c) shows the effect of sidelobes due to precipitation signals of 20- and 30-dB (SNR) powers, respectively. The windowed Fourier estimator is accurate with a precipitation signal of 10 dB (SNR), as with the Fourier estimator, and does not show the sidelobe effect even with 20- and 30-dB (SNR) power signals. Spectral broadening brought by the window function is not significantly seen in any of the plots of Fig. 3. The Capon estimator, despite the approximation of 8, works in these simulations. In the Capon DPS, underestimations are seen particularly around 4-m/s Doppler velocity in Fig. 3(a) and 6 m/s in Fig. 3(b). It is considered that these were caused by the principle of the Capon estimator, that is, the minimum power estimation. The Capon estimator, moreover, produced sidelobes smaller than those of the Fourier estimator, as can be seen around Doppler velocities of 13 m/s in Fig. 3(c). The MMSE DPSs show underestimations similar to the Capon DPSs [see around 6 m/s in Fig. 3(b)]. However, the effects of its sidelobes that are apparent in the Fourier and Capon estimations are not seen. Fig. 4(a) and (b) shows the examples of estimated DPSs from the simulated precipitation signals with spectral widths of 1 and 4 m/s, respectively. Since the simulation has SNR $=$ 10 dB and $N = 32$, Fig. 4 can be compared with Fig. 3(a). The MMSE estimator performs, as well as the other three estimators in cases with spectral widths representative of real-world observations.

Fig. 5(a)–(d) shows histograms comparing the reference with Fourier, windowed Fourier, Capon, and MMSE estimations, respectively. In these histograms, a single case corresponds to a single velocity component of a DPS. The histograms were created from two hundred simulations, which consisted of ten simulations for each mean velocity (0–19 m/s in 1-m/s increments). All simulations assumed precipitation signals with 10 dB (SNR), 2-m/s spectral width, and $N = 32$. Mean and standard errors between the references and the DPSs of the four estimators were calculated in dB by considering cases that were more than the noise level (0 dB) in the reference, that is, cases in the grayed areas were neglected. As indicated in the lower right side of each plot, mean errors of 0.17, 0.13, -1.51, and -0.94 dB resulted from the Fourier, windowed Fourier, Capon, and MMSE estimations, respectively. Their standard errors were 3.26, 3.58, 4.19, and 3.65 dB. Fig. 6 shows the dependencies of the mean and standard errors on SNR.

Fig. 6(a)–(c) were, respectively, obtained from simulations with precipitation spectral widths of 1, 2, and 4 m/s, that is, the mean and standard errors indicated in Fig. 5(a)–(d) appear in Fig. 6(b) at 10 dB (SNR). The Fourier estimator is accurate particularly with 0- or 10 dB (SNR) precipitation signals. With heavier precipitation, its high sidelobes increase the mean and standard errors. The largest mean and standard errors of about 3 dB and 6 dB, respectively, are seen in the 1-m/s spectral width, 30 dB (SNR) case. The windowed Fourier estimator is accurate with 0- or 10-dB (SNR) precipitation signals, similar to the Fourier estimator, and with 20- or 30-dB (SNR) precipitation signals, its mean errors are suppressed compared with the Fourier estimator because of its sidelobe reduction. Its mean and standard errors are about 2 and 5 dB at maximum with a 1-m/s spectral width and the 30-dB (SNR) power signal, which are caused by the spectral broadening of the Hamming window. With the Capon estimator, negative mean errors appear, which are about 2.5 dB at largest. Although the negative errors decrease as SNR increases, they were considered to be canceled by positive errors brought about by sidelobes. The Capon estimator's standard errors are the largest of the estimators for most of the spectral width and SNR combinations simulated. The MMSE estimator also shows negative errors, which are around 1 dB or less at spectral widths of 2 and 4 m/s. With a small spectral width of 1 m/s, however, the negative error reaches almost 2.5 dB with a 30-dB (SNR) precipitation signal. Regarding the standard error, the MMSE estimator is similar to the windowed Fourier estimator except for 1 m/s spectral width, and its standard deviations are similar to the Capon estimator in cases with 1-m/s spectral width.

Fig. 7(a) and (b) shows the mean and standard errors, supposing that $N = 64$ and 128, respectively. Since the spectral width was set to 2 m/s, these plots can be compared with Fig. 6(b). The Fourier, windowed Fourier, and MMSE estimators are improved by increasing N, while the Capon estimator is not improved so well. The resulting negative mean errors of the MMSE estimator are less than 1 dB. Fig. 8 shows the results from $N = 64$ and 128 simulations with 1-m/s spectral width and also shows the MMSE estimator's improvement more clearly.

2) DPSs With Ground Clutter: Fig. 9 shows examples of the estimated DPSs with ground clutter CNRs of 50 and 70 dB. The windowed Fourier estimator adopted the Hamming window for the simulations with a CNR of 50 dB and the Blackman window for a CNR of 70 dB. Since the simulations assumed $N = 32$ and precipitation signals with a power of 10 dB (SNR), a mean velocity of 4 m/s, and a spectral width of 2 m/s, the DPSs can be compared with Fig. 2, which has a 30-dB (CNR) ground clutter signal. The windowed

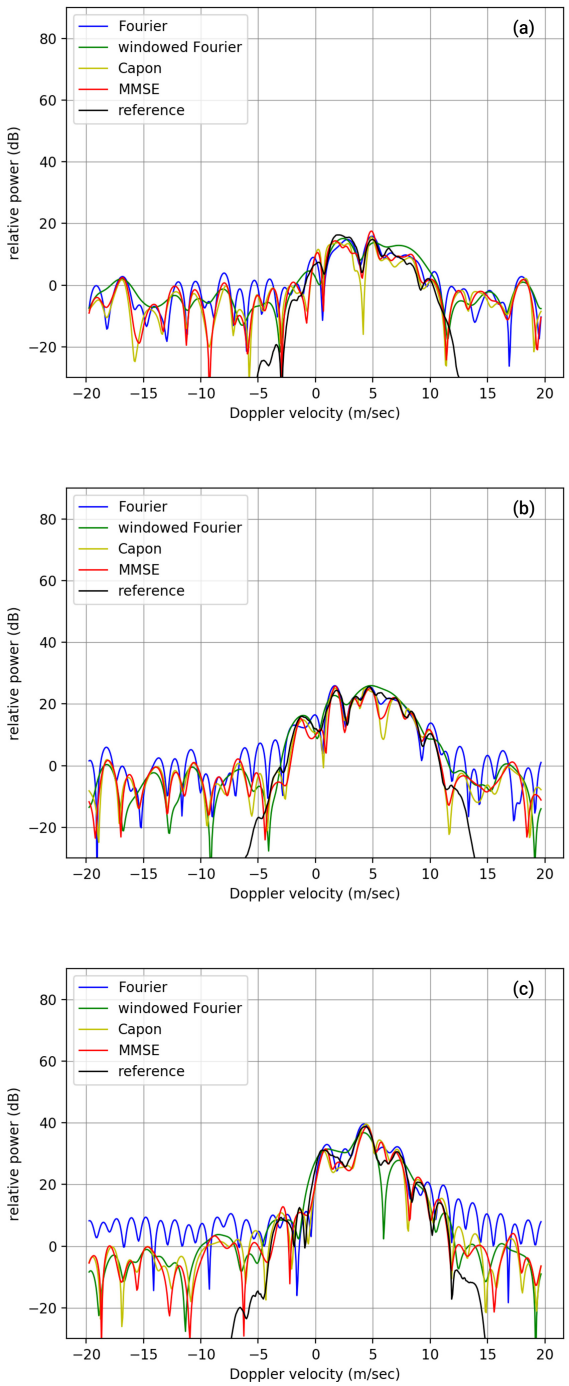

Fig. 3. Examples of DPS estimation results with $N = 32$ and a precipitation signal of mean velocity of 4 m/s, spectral width of 2 m/s, and powers of (a) 10 dB (SNR), (b) 20 dB (SNR), and (c) 30 dB (SNR).

Fourier estimator in Fig. 2 utilized the Hamming window. With the Fourier estimation, ground clutter contaminations due to sidelobes appear at a CNR of 30 dB, and their levels increase with CNR. The windowed Fourier estimator has lower ground clutter contaminations than the Fourier estimator, and any ground clutter contamination due to sidelobes is not observed in the 30-dB CNR simulation. However, the contaminations appear in the 50-dB CNR simulation. At a ground clutter power of 70-dB CNR, they are not completely suppressed

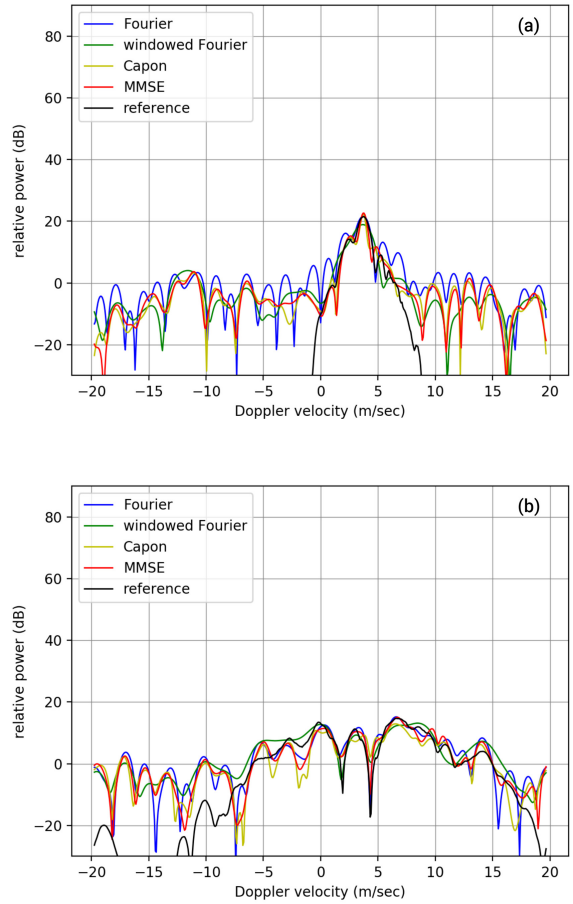

Fig. 4. Examples of DPS estimation results with $N = 32$ and a precipitation signal with a power of 10 dB, mean velocity of 4 m/s, and spectral widths of (a) 1 m/s and (b) 4 m/s.

to below the noise level even though the Blackman window was applied. Furthermore, the windowed Fourier estimator outputs the ground clutter signals more broadly around the zero velocity than the Fourier estimator, and the estimated ground clutter signals contaminate more velocity components of the precipitation signals. The ground clutter signals are even wider when using the Blackman window compared with using the Hamming window. With the Capon estimator, although the ground clutter signals are not broadened, its contaminations due to sidelobes appear. As shown in Figs. 2 and 9(a), the Capon estimator produces ground clutter contaminations due to sidelobes which are partially higher than the windowed Fourier estimator with the Hamming window. In Fig. 9(b), the ground clutter contaminations of the Capon estimator are higher than those of the Blackman-windowed Fourier estimator (when considering outside the broadened ground clutter signals of the windowed Fourier estimation). For the MMSE DPSs, meanwhile, ground clutter signals appear sharply around the zero velocity and do not cogenerate contaminations due to sidelobes. Precipitation signals are, therefore, represented by more noncontaminated velocity components than the other estimators. Fig. 10 shows how many velocity components of the MMSE DPSs are not contaminated by ground clutter, where the vertical axis indicates the mean

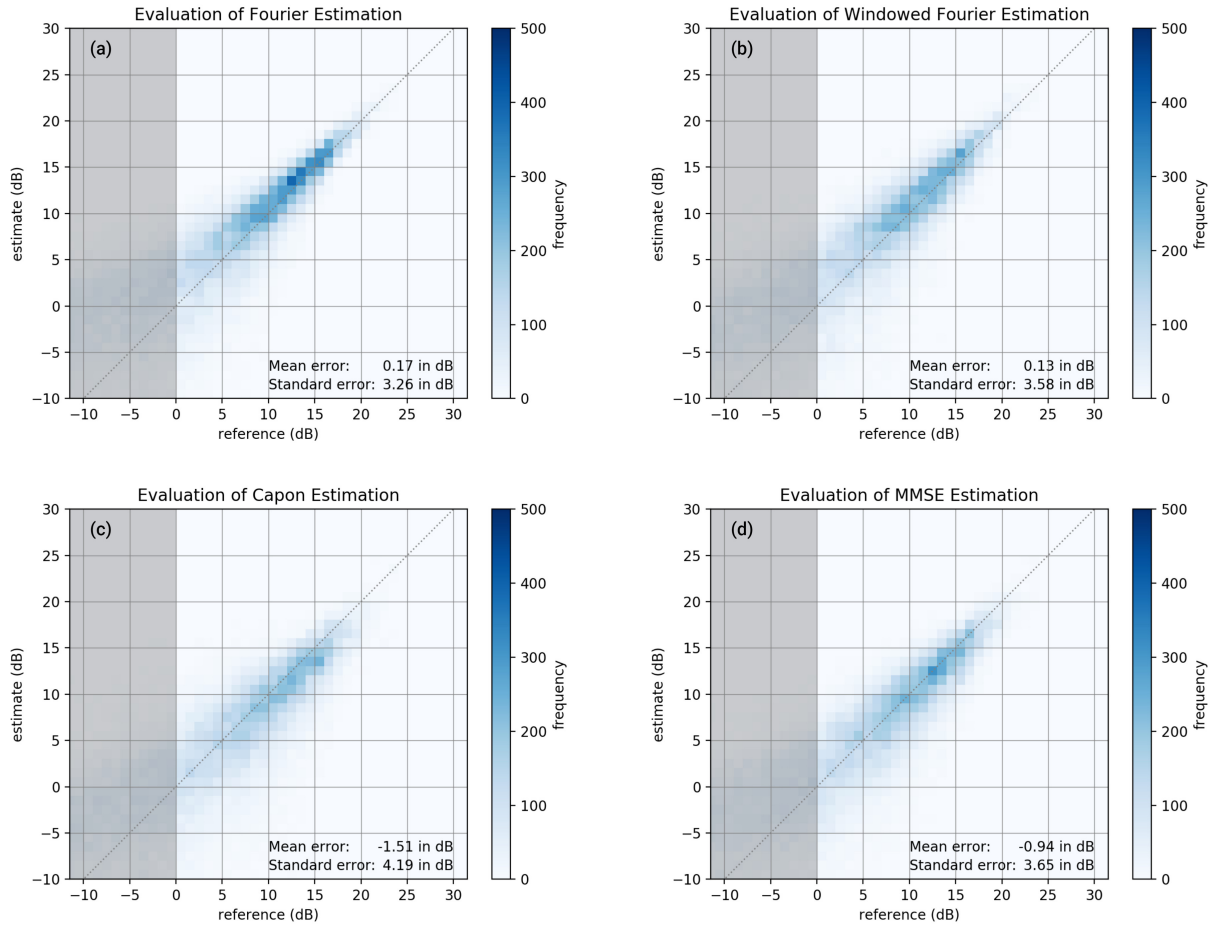

Fig. 5. Histograms comparing the reference with (a) Fourier estimation, (b) windowed Fourier estimation, (c) Capon estimation, and (d) MMSE estimation. Precipitation signals of 10 dB (SNR) and 4-m/s spectral width and $N = 32$ are assumed.

or standard error, and the horizontal axis is velocity (half) width for masking around-zero-velocity components. For example, errors at 2 m/s of the horizontal axis were calculated by excluding velocity components in the −2- to 2-m/s range. That is, Fig. 10 indicates that, by excluding a narrow velocity range of −2 – 2 m/s, the differences of the mean and standard error between the no ground clutter case and the case with a CNR of 70 dB were reduced to less than 1 dB and decrease further with decreasing CNR. Note that the mean and standard errors were calculated as in Section IV-C, that is, based on two hundred simulations with $N = 32$ and precipitation signals with 10 dB (SNR) and 2-m/s spectral width.

Fig. 11(a) and (b) shows ambiguity functions of the four estimators that were calculated when estimating a velocity component of 3.01 m/s in the simulations of Fig. 9(a) and (b), respectively. The ambiguity functions were derived as follows. Substituting (2) into (4) gives

$$\boldsymbol{x}^{[\mu]} = \boldsymbol{W}^{[\mu]\mathrm{H}}\boldsymbol{S}\boldsymbol{x} + \boldsymbol{W}^{[\mu]\mathrm{H}}\boldsymbol{n}. \tag{12}$$

The first term of the right side means that an element of $\boldsymbol{x}^{[\mu]}$ is calculated by an average of $\boldsymbol{x}$ weighted by a corresponding row of $\boldsymbol{W}^{[\mu]\mathrm{H}}\boldsymbol{S}$. For the m'th element of $\boldsymbol{x}^{[\mu]}$, the weights of the average are

$$\boldsymbol{\omega}_{m'}^{[\mu]} = \boldsymbol{S}^{\mathrm{H}}\boldsymbol{w}_{m'}^{[\mu]} \tag{13}$$

where $\boldsymbol{w}_{m'}^{[\mu]}$ is the m'th column of $\boldsymbol{W}^{[\mu]}$. The ambiguity functions for estimating the m'th element of $\boldsymbol{x}^{[\mu]}$ were calculated by applying the absolute square function to each element of $\boldsymbol{\omega}_{m'}^{[\mu]}$. All the four ambiguity functions have a mainlobe (around the desired velocity of 3.01 m/s) and sidelobes. The Fourier estimator is affected by ground clutter due to its high sidelobes in around-zero-velocity components. With the windowed Fourier estimator, although the sidelobes are suppressed compared to the Fourier estimator, the mainlobe is broadened. The Capon and MMSE estimators give adaptive weights that are small at around-zero velocities to cancel the effects of ground clutter, but the sidelobes out of around-zero velocities increase. However, such high sidelobes were not formed where precipitation signals existed, and their effects were suppressed in the 3.01-m/s velocity component. Since the MMSE estimator suppresses sidelobes around-zero velocities more than the Capon estimator, it is less affected by ground clutter, as ground clutter effects do not significantly appear in MMSE DPSs shown in Fig. 9.

D. Ground Clutter Analysis

Since signal simulation individually generated precipitation, ground clutter, and noise signals, a signal received only from ground clutter can also be created. By applying $\boldsymbol{W}^{[\mu]}$ to the

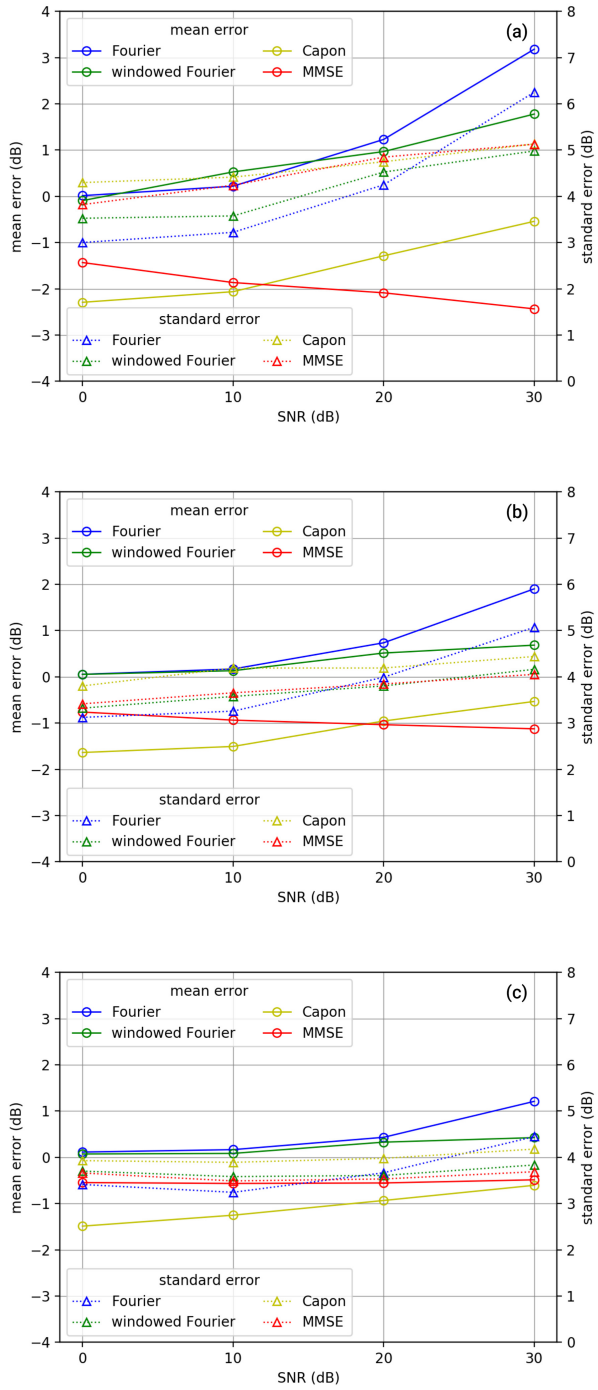

Fig. 6. Dependencies of mean and standard errors on SNR, evaluated assuming $N = 32$ and precipitation signals with spectral widths of (a) 1, (b) 2, and (c) 4 m/s.

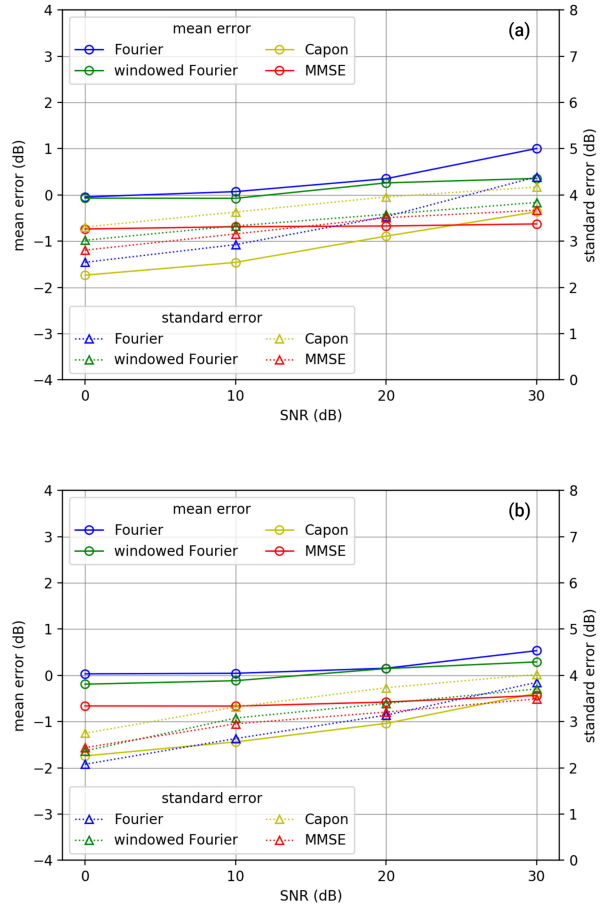

Fig. 7. Dependencies of mean and standard errors on SNR, evaluated by assuming precipitation signals with a spectral width of 2 m/s. (a) $N = 64$. (b) $N = 128$.

ground clutter signal, an estimated DPS of the ground clutter can be obtained, and the ground clutter DPS represents the width and severity of the ground clutter effects. Note that $\boldsymbol{W}^{[c]}$ and $\boldsymbol{W}^{[m]}$ must not be derived from the ground clutter signal but from received signals containing precipitation, ground clutter, and noise signals. Fig. 12 shows ground clutter DPSs produced by the four estimators. Since the ground clutter signals of Fig. 12(a) and (b) are, respectively, equal to those of Fig. 9(a) and (b), the velocity components around the zero velocity appear quite similar. In Fig. 12, the MMSE estimator outputs both the ground clutter signals sharply around the zero velocities and does not affect out of zero-velocity components as much as the other three estimators.

The ground clutter DPSs are quantitatively evaluated in Fig. 13. Fig. 13(a) shows the velocity widths of ground clutter signals as widths of ground clutter. The velocity widths were calculated as differences of two velocities at which power is -3 dB from the ground clutter peak level (-3-dB velocity range) in each of the DPSs; then, the velocity widths of two hundred DPSs were averaged arithmetically. Fig. 13(b) shows maximum and mean powers of velocity components less than -5 or more than 5 m/s as sidelobe levels. The maximum and mean powers in each of the two hundred DPSs were calculated and then averaged in dB. The two hundred simulations assumed $N = 32$ and precipitation signals of 10-dB power (SNR) and 2-m/s spectral width. In this evaluation, the precipitation signals affected only the Capon and MMSE estimators in the calculation of $\boldsymbol{W}^{[c]}$ and $\boldsymbol{W}^{[m]}$. The Fourier estimator does not produce spectral broadening, and it indicated widths around 1.1 m/s. Maximum and mean sidelobe levels were high in the Fourier estimation and increased with increasing CNR. Since the windowed Fourier estimator applied the Hamming window at CNRs of 30 and

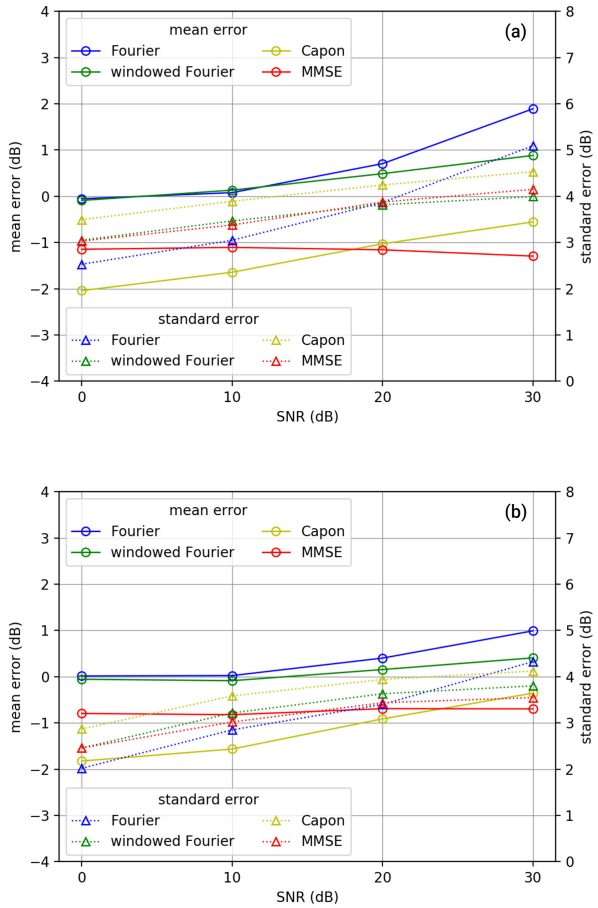

Fig. 8. Dependencies of mean and standard errors on SNR, evaluated by assuming precipitation signals with a spectral width of 1 m/s. (a) $N = 64$. (b) $N = 128$.

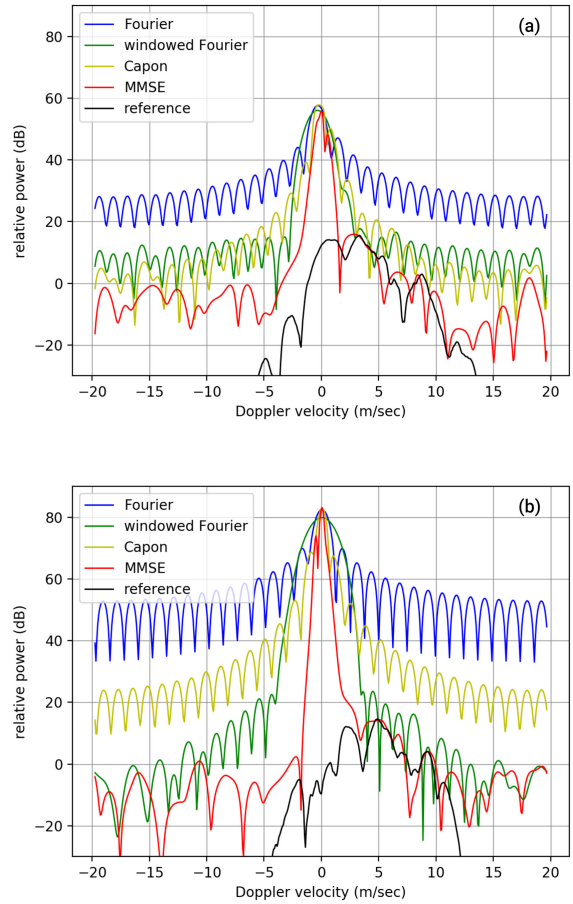

Fig. 9. Examples of DPS estimation results with $N = 32$, a precipitation signal of power 10 dB (SNR), mean velocity of 4 m/s, and spectral width of 2 m/s and a ground clutter signal of power (a) 50 dB (CNR) and (b) 70 dB (CNR).

50 dB and the Blackman window at 70 dB, its trend changed between 50 and 70 dB, which shows that the aggressive Blackman window suppressed sidelobe levels by sacrificing ground clutter width. The Capon estimator represented the ground clutter DPS with widths almost two times narrower than the Fourier estimator. Its maximum sidelobe levels were higher than that of the Hamming windowed Fourier estimator, and its mean sidelobe levels were lower than that of the Hamming but higher than that of the Blackman. In addition, its sidelobe levels increased along with CNR, as seen with the Fourier estimator. The MMSE estimator showed excellent characteristics compared with the other three estimators: the ground clutter widths were almost three times narrower than the Fourier estimator (about 0.4 m/s), and maximum and mean sidelobe levels were about −10 and −20 dB, respectively. The maximum and mean sidelobe levels in the MMSE estimation, furthermore, were hardly affected by the increase in CNR.

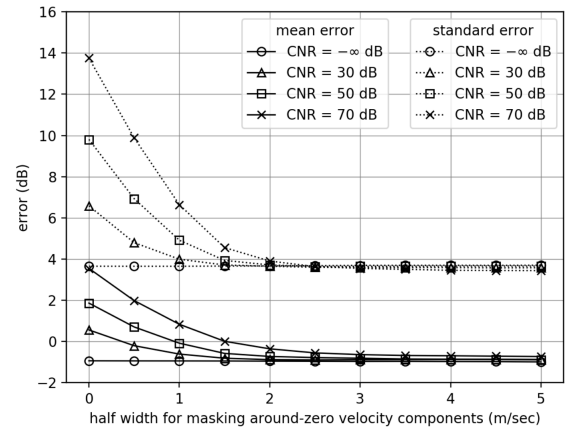

Fig. 10. Mean and standard errors of the MMSE estimator calculated by excluding around zero-velocity components. Evaluations based on simulations with precipitation signals of power of 10 dB (SNR) and spectral width of 2 m/s.

E. Computational Complexity

As explained in Section III-C, the first step of the MMSE estimation is equivalent to the Fourier estimation. Each of its iteration steps is similar to the Capon estimation in computational complexity because a single $N \times N$ matrix inversion dominates both the calculations. Thus, the computational complexity of the MMSE estimator can be roughly estimated from the number of iterations steps carried out in the simulation.

Fig. 14 shows the number of the iteration steps in the simulations that were implemented in Section IV-C. Looking

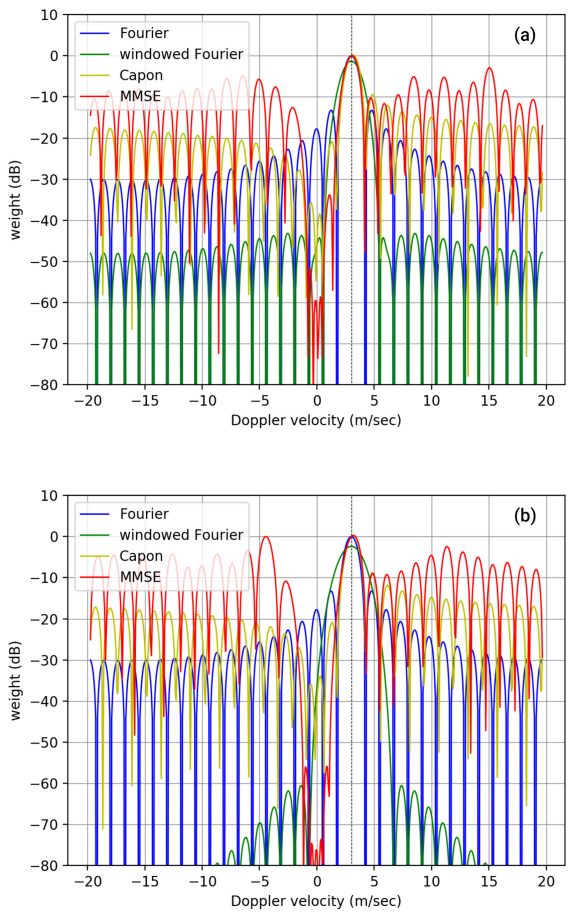

Fig. 11. Ambiguity functions for estimating a velocity component of 3.01 m/s in the simulation shown in Fig. 9. (a) and (b) corresponds to Fig. 9(a) and (b), respectively.

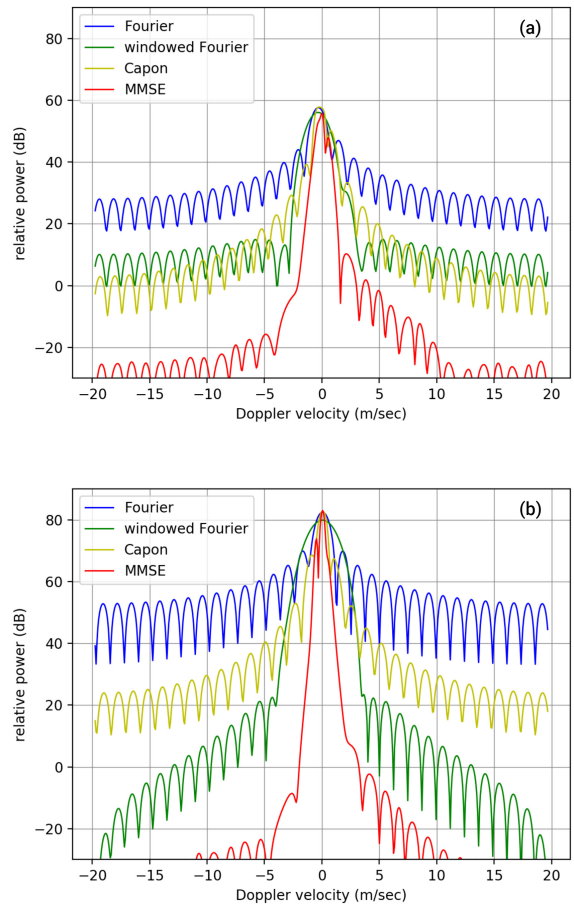

Fig. 12. Examples of DPS estimation results in which ground clutter DPSs were extracted from DPSs of Fig. 9. (a) and (b) corresponds to Fig. 9(a) and (b), respectively.

at simulations assuming precipitation signals with 10 dB (SNR) and 2-m/s spectral width, the mean, standard deviation, and maximum values of the number of iterations, steps were calculated for each combination of CNR and the number of transmitted pulses (N). Similar to Section IV-C, these statistical values were calculated from two hundred simulations. For each N, all the statistical values increase with increasing CNR. This is probably because large numbers of iteration steps are needed to reduce the large sidelobe contaminations. On the other hand, the number of iterations seems to be independent of N.

V. Demonstration

The MMSE estimator was demonstrated by applying it to the actual received signal from a phased PAWR [8]. The signal was received at an azimuthal angle of 180.37° and an elevation angle of 0.00° and was obtained at 16:55:31 on August 7, 2017. Five adjacent range gates were averaged for calculating $\boldsymbol{R}_{(l)}$. Fig. 15(a)–(c) shows spectrographs derived from the Fourier, windowed Fourier, and MMSE estimators, respectively. The windowed Fourier estimator adopted the Hamming window. The horizontal and vertical axes, respectively, indicate the velocity and distance relative to the PAWR.

The demonstration results in Fig. 15 are consistent with the results of the simulations in Section IV; that is, the Fourier estimator leads to heavy contaminations due to its sidelobes, the windowed Fourier estimator suppresses sidelobes but results in a spectral broadening of ground clutter signals, and the MMSE estimator estimates ground clutter with a narrow width and low contaminations by sidelobes and precipitation signals are more clearly detectable than with the Fourier and the windowed Fourier estimations. In the MMSE spectrograph, however, ground clutter contaminations caused by sidelobes are seen at a few range gates roughly around 15 and 17.5 km, which is larger than those in the windowed Fourier spectrograph. Although the large contaminations disappear when using a single received signal for the calculation of $\boldsymbol{R}_{(l)}$, the MMSE estimator causes a large underestimation just with a single received signal, as discussed in Section VI.

VI. Discussion

The simulations and demonstration described in Section IV and V, respectively, show that, with five independent received signals, the MMSE estimator performs as well the Fourier, windowed Fourier, and Capon estimators in cases with no ground clutter and much better when ground clutter is present. As mentioned in Section III-C, the number of independent received signals relates to the approximation accuracy of $\boldsymbol{R}_{(l)}$.

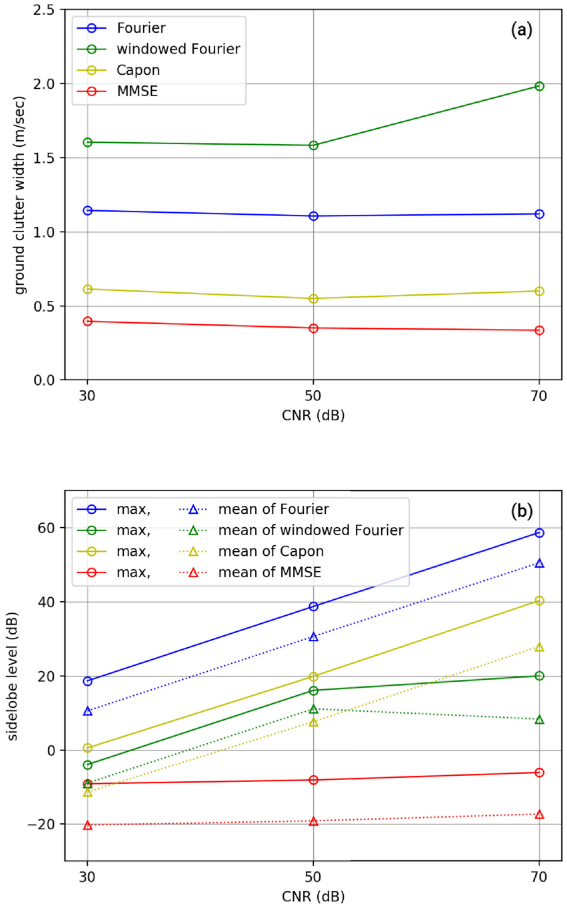

Fig. 13. Effects of ground clutter. (a) Ground clutter width. (b) Maximum and mean sidelobe levels due to ground clutter.

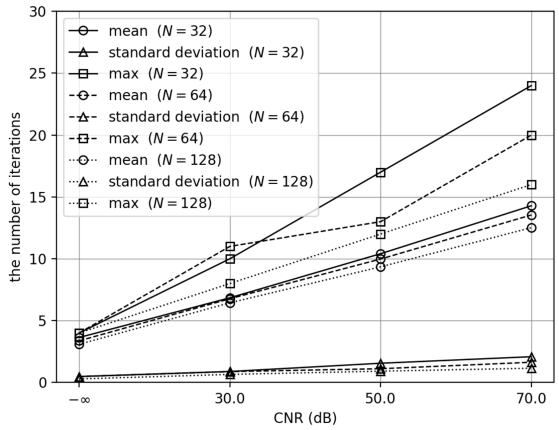

Fig. 14. Computational complexities of the MMSE estimator estimated by the number of iterations, which were calculated in simulations with a precipitation signal of 10-dB (SNR) power and 4-m/s mean velocity.

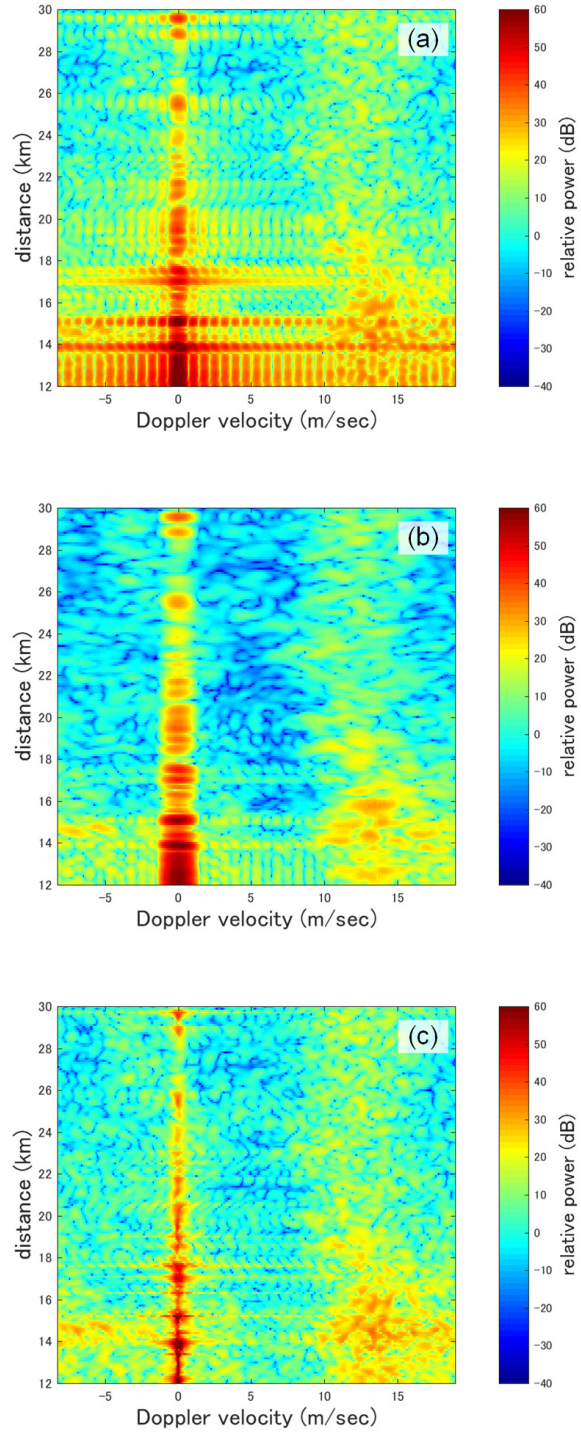

Fig. 15. Spectrographs derived from the received signal from a PAWR by applying (a) Fourier estimator, (b) windowed Fourier estimator, and (c) MMSE estimator.

This section discusses the MMSE estimation accuracy with respect to $\boldsymbol{R}_{(l)}$.

Fig. 16 shows the relationship between the number of independent received signals and the MMSE estimator's mean and standard errors, which were derived from simulations performed in Section IV. In the evaluation, simulations supposing $N = 32$, no ground clutter, and precipitation signals with a spectral width of 2 m/s were considered. Both mean and standard errors were improved by increasing the number of received signals. The errors were rapidly reduced by increasing the number of received signals from one to three and almost converged after five.

The accurate approximation of $\boldsymbol{R}_{(l)}$ might not be realized when there is a drastic change in the range profile of ground

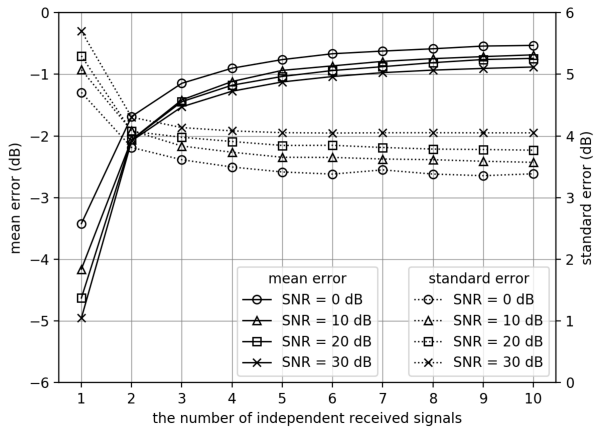

Fig. 16. Mean and standard errors as functions of the number of independent received signals, which were calculated by simulations of a precipitation signal of 2 m/s spectral width and no ground clutter signal.

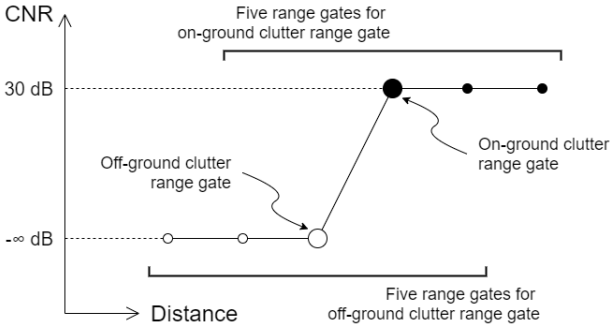

Fig. 17. Description of off- and on-ground clutter range gates for evaluating effects of a drastic change of CNR with the distance to the MMSE estimator.

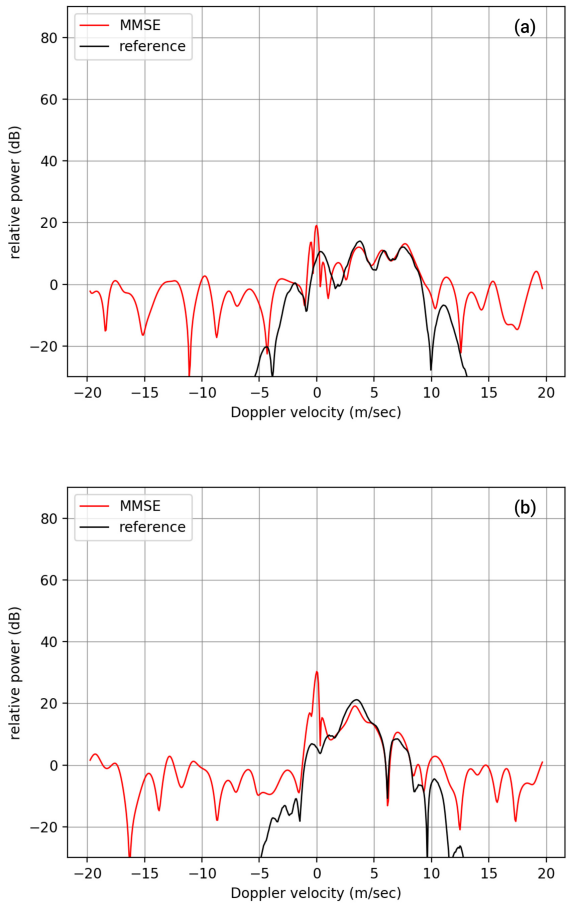

Fig. 18. Examples of MMSE DPSs in (a) off- and (b) on-ground clutter range gates. A precipitation signal of 10-dB (SNR) power, 4-m/s mean velocity, and 2-m/s spectral width and a ground clutter signal of 30-dB (CNR) power were assumed.

clutter. We evaluate this by supposing a step change of CNR (from $-\infty$ to 30 dB), as described in Fig. 17. The received signals at a range gate that is an edge of off-ground clutter (clutter absent) and on-ground clutter (clutter present) conditions were simulated, and DPSs were estimated from the received signals. Fig. 18(a) and (b) shows the DPSs at the off- and on-ground clutter range gates, respectively. Since parameters of $N = 32$ and precipitation signals with a power of 10 dB (SNR), a mean velocity of 4 m/s, and a spectral width of 2 m/s are supposed, they can be compared with Fig. 2. In the off-ground clutter range gate [see Fig. 18(a)], errors appeared around the zero velocity, which were produced by wrongly formed ambiguity functions. Also, in the on-ground clutter range gate [see Fig. 18(b)], the ground clutter signal is seen because the MMSE estimator did not sufficiently reduce its sidelobes around the zero velocity. Their peak levels at the zero velocity were roughly 20 and 30 dB that are smaller than that of Fig. 2 (40 dB). This is qualitatively consistent with Fig. 15. Fig. 15(a) and (b) shows a gap of ground clutter at a distance of 18 km. In Fig. 15(c), on the other hand, no such gap is seen, and ground clutters around the distance seem to be weakened. It is also considered that the ground clutter contaminations roughly around 15 and 17.5 km were produced by the same mechanism as the on-ground clutter range gate. Similar effects can happen in the Capon estimation when it uses multiple range gates for the approximation of 8.

VII. Conclusion

It was shown in [13] that an MMSE estimator gives phased-array digital beamforming with high performance. In contrast to the Fourier estimator for phased-array digital beamforming, the MMSE estimator suppresses contaminations that are cogenerated with strong echoes by antenna sidelobes and accurately estimates the angular profile of received power. Since phased-array digital beamforming is mathematically equivalent to weather radar Doppler spectral analysis, the MMSE estimator can also be used for that application. In the Doppler spectral analysis of weather radars, strong ground clutter signal contaminate all velocity components of the DPS, particularly when observing at low elevation angles. Since hazardous severe weather phenomena occur at low altitudes, the contaminations due to strong ground clutter should be suppressed to allow earlier detection and warning of low-altitude hazardous weather phenomena over wide areas.

The MMSE estimator was applied to simulated weather-radar received signals, and its estimated DPSs were compared with those of the traditional Fourier and

windowed Fourier estimators and the Capon's adaptive spectral estimator. The MMSE estimated DPSs were confirmed to be almost as accurate as those of the other three estimators in simulations with no ground clutter. With ground clutter, they gave greater suppression of sidelobes and sharper estimation of the ground clutter. Specifically, strong ground clutter signals with 70 dB (CNR) appeared in a narrow range of Doppler velocities of −2–2 m/s and caused the mean and standard errors of velocity components out of −2–2 m/s to deteriorate by less than 1 dB (in simulations with 32 transmitted pulses with a sampling frequency of 2.5 kHz). Meanwhile, the Fourier, windowed Fourier, and Capon DPSs estimated from the same received signals were dominated by strong ground clutter with a CNR of greater than 30 dB. Note that, for a small precipitation spectral width of 1 m/s, with $N = 32$, the MMSE estimator has performed with negative bias errors that are larger than the three other estimators. This inaccuracy was reduced with longer received signals of $N = 64$ or 128. When an ambiguity function's mainlobe width (which is determined by the temporal length of a received signal) is similar to or broader than a spectral width of a precipitation signal, the precipitation signal is narrowly estimated by the MMSE estimator, which results in the negative bias errors.

The result of a demonstration in which the MMSE estimator was applied to actual weather radar observation signals was similar to the simulations: the MMSE estimator output sidelobeless DPSs with no spectral broadening, while the Fourier estimator DPS was underground clutter contaminations due to sidelobes and the windowed Fourier estimator produced spectral broadening. The MMSE estimator has a disadvantage of requiring several received signals. In the demonstration, the MMSE estimator was implemented with received signals obtained at five adjacent range gates. Although the disadvantage was not very apparent in the demonstration, it can be problematic especially when a ground clutter range profile drastically changes.

Appendix A
Phased Array Beamforming and Doppler Spectral Analysis

Supposing a 1-D phased array with geometry shown in Fig. 19, the governing equation of phased array beamforming is

$$\boldsymbol{\zeta} \approx \boldsymbol{\Phi}\boldsymbol{\xi} + \boldsymbol{\delta} \tag{14}$$

where $\boldsymbol{\zeta} = \left[\zeta^{(1)}\ \zeta^{(2)}\ \ldots\ \zeta^{(n_p)}\ \ldots\ \zeta^{(N_p)}\right]^{\mathrm{T}}$ and $\zeta^{(n_p)}$ is a signal received by the n_pth antenna element at an arbitrary time (snap shot). $\boldsymbol{\delta}$ represents additional noises on the antenna elements. $\boldsymbol{\xi} = \left[\xi_{-M_p/2}\ \xi_{-M_p/2+1}\ \ldots\ \xi_{m_p}\ \ldots\ \xi_{M_p/2-1}\right]^{\mathrm{T}}$ digitally represents an angle profile of targets' scattering (complex) amplitude. Note that $\boldsymbol{\xi}$ includes effects of radio propagation, such as attenuation and absorption along the propagation path. $\boldsymbol{\Phi}$ is an $N_p \times M_p$ matrix that represents phase delays between rays from targets to antenna elements. Here, assume that rays from each target are parallel; that is, the targets are assumed to be far from the antenna. Its m_pth column $\boldsymbol{\phi}_{m_p}$ is

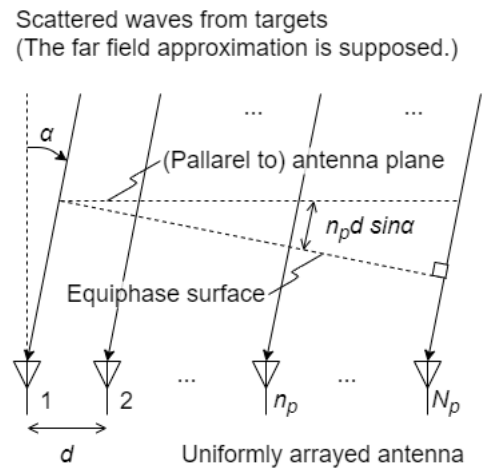

Fig. 19. Geometry of a 1-D phased array antenna.

an N_p-vector of which the n_pth element is given by $\phi_{m_p}^{(n_p)} = \exp\{j2\pi(d/\lambda)n_p \sin\alpha_{m_p}\}$, where d is an interval of each pair of adjacent antenna elements and λ is the wavelength of the radiated wave. α_{m_p} is the m_pth angle from the perpendicular direction.

When $(1/2)\sin\alpha_{m_p} = m_p/M_p$ is applied, $\phi_{m_p}^{(n_p)} = \exp\{j2\pi m_p(2\lambda^{-1}/M_p)n_p d\}$. Comparing $\phi_{m_p}^{(n_p)}$ of 14 with $s_m^{(n)}$ of 2 (or 3), $2\lambda^{-1}/M_p$ and d in phased array beamforming correspond to Δ_f and Δ_t in the Doppler spectral analysis, respectively. Thus, phased array beamforming is mathematically equivalent to the Doppler spectral analysis. Note that both linear equations of 14 and 3 are approximately established, and their approximations differ from each other. These correspondences are, in other words, that time- and frequency-axes in the Doppler spectral analysis are equivalent to the spatial axis of an arrayed antenna and the angle axis, respectively. Therefore, all digital signal processing methods of the Doppler spectral analysis can be applied to an arrayed antenna with digital beamforming, and vice versa. The spectral mainlobe and sidelobes in the Doppler spectral analysis are equivalent to those of an arrayed antenna. Aliasing in the Doppler spectral analysis is to grating lobe in phased array beamforming. While this equivalence was presented by D. H. Johnson [19], this appendix represented it digitally by using a matrix formulation, which is more familiar to recent digital systems.

Appendix B
Comparison to the AR Estimator

The AR estimator, which is also called the maximum entropy method, supposes that signals are based on an AR random process model. Fig. 20 compares the AR estimator with the Fourier and MMSE estimators in a simulation, which is the same as that in Fig. 2. The AR estimation was implemented by solving the Yule–Walker equation with orders of 8 and 31 by supposing to have five independent received signals (see [14] for details of the AR estimator). In the two AR estimations, the ground clutter signal sharply appeared. Velocity components out of around-zero velocities are seen

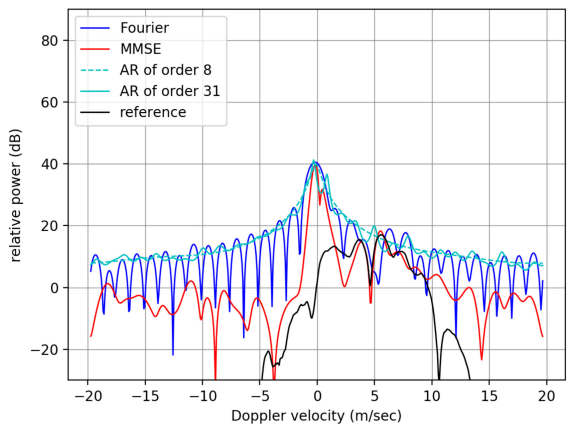

Fig. 20. Comparison of the AR DPSs with orders of 8 and 31 to the Fourier and MMSE DPSs in a simulation supposing $N = 32$. A precipitation signal of 10-dB (SNR) power, 4-m/s mean velocity, and 2-m/s spectral width and a ground clutter signal of 30-dB (CNR) power were assumed.

with levels similar to sidelobe peaks of the Fourier estimators. The precipitation signal was, therefore, not detectable, as well as the MMSE estimator.

Acknowledgment

The authors would like to thank Dr. Toshio Iguchi of the National Institute of Information and Communications Technology and Dr. Koji Nishimura of the National Institute of Polar Research for fruitful discussions.

References

[1] D. Atlas, *Radar in Meteorology*. Boston, MA, USA: American Meteorological Society, 1990.

[2] F. Junyent and V. Chandrasekar, "Theory and characterization of weather radar networks," *J. Atmos. Ocean. Technol.*, vol. 26, no. 3, pp. 474–491, Mar. 2009.

[3] V. Chandrasekar, H. Chen, and B. Philips, "DFW urban radar network observations of floods, tornadoes and hail storms," in *Proc. IEEE Radar Conf. (RadarConf)*, Oklahoma City, OK, USA, Apr. 2018, pp. 0765–0770.

[4] M. Maki *et al.*, "Semi-operational rainfall observations with X-band multi-parameter radar," *Atmos. Sci. Lett.*, vol. 6, no. 1, pp. 12–18, Jan./Mar. 2005.

[5] T. Mega, K. Monden, T. Ushio, K. Okamoto, Z. Kawasaki, and T. Morimoto, "A low-power high-resolution broad-band radar using a pulse compression technique for meteorological application," *IEEE Geosci. Remote Sens. Lett.*, vol. 4, no. 3, pp. 392–396, Jul. 2007.

[6] E. Yoshikawa *et al.*, "Development and initial observation of high-resolution volume-scanning radar for meteorological application," *IEEE Trans. Geosci. Remote Sens.*, vol. 48, no. 8, pp. 3225–3235, Aug. 2010.

[7] E. Yoshikawa, T. Ushio, Z. Kawasaki, and V. Chandrasekar, "Dual-directional radar observation for preliminary assessment of the ku-band broadband radar network," *J. Atmos. Ocean. Technol.*, vol. 29, no. 12, pp. 1757–1768, 2012.

[8] F. Mizutani *et al.*, "Fast-scanning phased-array weather radar with angular imaging technique," *IEEE Trans. Geosci. Remote Sens.*, vol. 56, no. 5, pp. 2664–2673, May 2018.

[9] R. J. Doviak and D. S. Zrnic, *Doppler Radar and Weather Observations*, 2nd ed. New York, NY, USA: Dover, 1984.

[10] B. D. Carlson, "Covariance matrix estimation errors and diagonal loading in adaptive arrays," *IEEE Trans. Aerosp. Electron. Syst.*, vol. 24, no. 4, pp. 397–401, Jul. 1988, doi: 10.1109/7.7181.

[11] A. Siggia and J. R. Passarelli, "Gaussian model adaptive processing (GMAP) for improved ground clutter cancellation and moment calculation," in *Proc. 3rd Eur. Conf. Radar Meteorol. Hydrol.*, Gotland, Sweden, 2004, pp. 67–73.

[12] J. Capon, "High-resolution frequency-wavenumber spectrum analysis," *Proc. IEEE*, vol. 57, no. 8, pp. 1408–1418, Aug. 1969.

[13] E. Yoshikawa *et al.*, "MMSE beam forming on fast-scanning phased array weather radar," *IEEE Trans. Geosci. Remote Sens.*, vol. 51, no. 5, pp. 3077–3088, May 2013.

[14] P. Stoica and R. L. Moses, *Introduction to Spectral Analysis*. Upper Saddle River, NJ, USA: Prentice-Hall, 1977.

[15] D. S. Zrnić, "Simulation of weatherlike Doppler spectra and signals," *J. Appl. Meteorol.*, vol. 14, no. 4, pp. 619–620, Jan. 1975.

[16] V. Chandrasekar, V. N. Bringi, P. Brockwell, "Statistical properties of dual-polarized radar signals," in *Proc. 23rd Conf. Radar Meteorol.*, 1986, pp. 193–196.

[17] A. V. Oppenheim and R. W. Schafer, *Discrete-Time Signal Processing*, 3rd ed., Harlow, U.K.: Pearson, 2014.

[18] R. C. Hansen, *Phased Array Antennas*, 2nd ed. John Hoboken, NJ, USA: Wiley, 2009.

[19] D. H. Johnson, "The application of spectral estimation methods to bearing estimation problems," *Proc. IEEE*, vol. 70, no. 9, pp. 1018–1028, Sep. 1982.

[20] V. N. Bringi and V. Chandrasekar, *Polarimetric Doppler Weather Radar: Principles and Applications*. Cambridge, U.K.: Cambridge Univ. Press, 2001.

Eiichi Yoshikawa received the B.E. degree from the Department of Aerospace Engineering, Osaka Prefecture University, Sakai, Japan, in 2005, and the M.E. and Ph.D. degrees from the Division of Electrical, Electronic and Information Engineering, Osaka University, Suita, Japan, in 2008 and 2011, respectively.

In 2011, he was a Post-Doctoral Researcher with Osaka University and Colorado State University, Fort Collins, CO, USA, and also a Post-Doctoral Fellow of the Research Fellowship for Young Scientists sponsored by the Japan Society for the Promotion of Science. In 2012, he joined the Japan Aerospace Exploration Agency, Mitaka, Japan, where he is an Associate Senior Researcher. He concurrently serves as a Visiting Associate Professor with Tokyo Metropolitan University, Hino, Japan. His research interests include weather radar remote sensing, radar-based analyses, and applications for general and aviation weather.

Naoya Takizawa received the B.E. degree from the Department of Aeronautics and Astronautics, Tokyo Metropolitan University, Hino, Japan, in 2018, where he is pursuing the master's degree with the Department of Aeronautics and Astronautics.

His research interests include weather radar remote sensing and the development of radar systems.

Hiroshi Kikuchi (Member, IEEE) received the B.S. degree from the Department of Engineering, Doshisha University, Kyoto, Japan, in 2008, and the M.S. and Ph.D. degrees from the Division of Electrical, Electronic and Information Engineering, Osaka University, Suita, Japan, in 2010 and 2013, respectively.

He joined the Division of Electrical, Electric and Information Engineering, Osaka University as a Specially Appointed Researcher in 2013. In 2017, he was a Research Assistant Professor with Tokyo Metropolitan University, Hino, Japan. In 2018, he joined The University of Electro-Communications, where he is an Assistant Professor. His research specialties are remote sensing for atmospheric electricity with spaceborne platforms, and weather radar remote sensing and the development of the radar system.

Tomoaki Mega received the B.S., M.S., and Ph.D. degrees in aerospace engineering from Osaka Prefecture University, Sakai, Japan, in 2001, 2003, and 2008, respectively.

From 2008 to 2011, he was a Post-Doctoral Fellow with the Research Institute of Sustainable Humanosphere, Kyoto University, Kyoto, Japan, where he was a Post-Doctoral Fellow with the Graduate School of Science, from 2011 to 2013. From 2013 to 2017, he was a Post-Doctoral Fellow with Osaka University, Suita, Japan. From 2017 to 2019, he was a Research Associate Professor with the Graduate School of System Design, Tokyo Metropolitan University, Hino, Japan. From 2019 to 2020, he was a Specially Appointed Associate Professor with the Graduate School of Engineering, Osaka University. Since 2020, he has been a Specially Appointed Assistant Professor with the Graduate School of Engineering, Osaka University. His research interests include algorithm development for spaceborne microwave radiometers and validation of rainfall retrievals.

Tomoo Ushio (Senior Member, IEEE) received the B.S., M.S., and Ph.D. degrees in electrical engineering from Osaka University, Suita, Japan, in 1993, 1995, 1998, respectively.

He was with the Global Hydrology and Climate Center, Huntsville, AL, USA, as a Post-Doctoral Researcher from 1998 to 2000. In 2000, he joined the Department of Aerospace Engineering, Osaka Prefecture University, Sakai, Japan. In 2006, he was with the Department of Electrical, Electronic and Infocommunication Engineering, Osaka University as an Associate Professor, where he is a Professor. His research specialties are radar-based remote sensing, passive and active remote sensing of the atmosphere from spaceborne platforms, and atmospheric electricity.